Comparison of Tomo-PIV Versus Dual Plane PIV on a Synthetic Jet Flow

Mark P. Wernet
Glenn Research Center, Cleveland, Ohio

NASA STI Program . . . in Profile

Since its founding, NASA has been dedicated to the advancement of aeronautics and space science. The NASA Scientific and Technical Information (STI) Program plays a key part in helping NASA maintain this important role.

The NASA STI Program operates under the auspices of the Agency Chief Information Officer. It collects, organizes, provides for archiving, and disseminates NASA's STI. The NASA STI Program provides access to the NASA Technical Report Server—Registered (NTRS Reg) and NASA Technical Report Server—Public (NTRS) thus providing one of the largest collections of aeronautical and space science STI in the world. Results are published in both non-NASA channels and by NASA in the NASA STI Report Series, which includes the following report types:

- TECHNICAL PUBLICATION. Reports of completed research or a major significant phase of research that present the results of NASA programs and include extensive data or theoretical analysis. Includes compilations of significant scientific and technical data and information deemed to be of continuing reference value. NASA counter-part of peer-reviewed formal professional papers, but has less stringent limitations on manuscript length and extent of graphic presentations.

- TECHNICAL MEMORANDUM. Scientific and technical findings that are preliminary or of specialized interest, e.g., "quick-release" reports, working papers, and bibliographies that contain minimal annotation. Does not contain extensive analysis.

- CONTRACTOR REPORT. Scientific and technical findings by NASA-sponsored contractors and grantees.

- CONFERENCE PUBLICATION. Collected papers from scientific and technical conferences, symposia, seminars, or other meetings sponsored or co-sponsored by NASA.

- SPECIAL PUBLICATION. Scientific, technical, or historical information from NASA programs, projects, and missions, often concerned with subjects having substantial public interest.

- TECHNICAL TRANSLATION. English-language translations of foreign scientific and technical material pertinent to NASA's mission.

For more information about the NASA STI program, see the following:

- Access the NASA STI program home page at http://www.sti.nasa.gov

- E-mail your question to help@sti.nasa.gov

- Fax your question to the NASA STI Information Desk at 757-864-6500

- Telephone the NASA STI Information Desk at 757-864-9658

- Write to:
  NASA STI Program
  Mail Stop 148
  NASA Langley Research Center
  Hampton, VA 23681-2199

Comparison of Tomo-PIV Versus Dual Plane PIV on a Synthetic Jet Flow

Mark P. Wernet
Glenn Research Center, Cleveland, Ohio

National Aeronautics and
Space Administration

Glenn Research Center
Cleveland, Ohio 44135

May 2017

Acknowledgments

Level of Review: This material has been technically reviewed by technical management.

Comparison of Tomo-PIV Versus Dual Plane PIV on a Synthetic Jet Flow

Mark P. Wernet
National Aeronautics and Space Administration
Glenn Research Center
Cleveland, Ohio 44135

Abstract

Particle Imaging Velocimetry (PIV) is a planar velocity measurement technique that has found widespread use across a wide class of engineering disciplines. Tomographic PIV (Tomo-PIV) is an extension of the traditional PIV technique whereby the velocity across a volume of fluid is measured. Tomo-PIV provides additional fluid mechanical properties of the flow due to the adjacent planes of velocity information that are extracted. Dual Plane PIV is another approach for providing cross-plane flow field properties. Dual Plane PIV and Tomo-PIV provide all of the same flow properties, albeit through very different routes with significantly different levels of effort, hence a comparison of their application and performance would prove beneficial in a well-known, highly 3D flow field. A synthetic jet flow which has a wide range of flow field features including high velocity gradients and regions of high vorticity was used as a rigorous test bed to determine the capabilities/limitations of the Dual Plane PIV and Tomo-PIV techniques. The results show that compressing 3D particle field information down to a limited number of views does not permit the accurate reconstruction of the flow field in regions of high velocity gradients. The traditional thin sheet techniques are the best approach for accurate flow field measurements.

Nomenclature

2C PIV	2-component Particle Imaging Velocimetry
CAD	Computer Aided Drafting
CFD	Computation Fluid Dynamics
DVM	Digital Volt Meter
MART	Multiplicative Algebraic Reconstruction Technique
RMS	Root Mean Square
SNR	Signal to Noise Ratio
SPIV	Stereo PIV
TTL	Transistor-Transistor Logic
L/D	Ratio of the glass chamber dimension to the synthetic jet exit port diameter
ppp	Particles per pixel [#particles/pixel]
u,v,w	Components of velocity along the x-, y-, and z-coordinate axes
ω_z	z-component of vorticity [1/s]
ω_x	x-component of vorticity [1/s]

Introduction

Particle Imaging Velocimetry (PIV) is a well-established technique for measuring flow field properties across extended planar domains. The wide use and long development time of the PIV technique has led to its application to a wide variety of engineering problems and its ability to provide high precision flow measurements. PIV has been effectively used at NASA GRC over the past 20 years in a wide range of applications including axial and centrifugal compressors, pulse detonation engines, supersonic parachute flows, jet plume/shock interactions, aeroacoustics, launch abort systems testing, mechanical heart valves, chicken embryo blood flow and microgravity flows. The motivation for these PIV measurements is in support of Computational Fluid Dynamics (CFD) code development, where the modelers are interested in as many of the flow field properties that can be measured in order to assess the fidelity of their flow field predictions and the underlying turbulence models. Tomographic PIV (Tomo-PIV) is a newer approach for acquiring and extracting velocity information across extended volumes of a flow field, enabling computation of additional fluid mechanical properties (Ref. 1). Tomo-PIV can provide volumetric flow information by simply adding more camera views to a traditional stereo PIV system and then applying computationally intensive processing algorithms requiring significant processing times (days or weeks) to complete. An alternative to Tomo-PIV is Dual-Plane PIV, which essentially uses two Stereo PIV systems with their laser light sheets closely spaced in the flow (Refs. 2 and 3). Dual Plane PIV is slightly more complex to setup, but the data reduction is straight forward and fast.

Traditional PIV and Stereo PIV (SPIV) provide 2-component and 3-component velocity measurements across a single plane in the flow. These two techniques are widely used and are capable of providing high spatial resolution, high accuracy velocity estimates. The appeal of Tomo-PIV and Dual Plane PIV stems from their ability to provide both in-plane and cross-plane flow properties, such as all 3-components of vorticity. A comprehensive and thorough review of the Tomo-PIV technique covering the various camera configurations, tomographic reconstruction algorithms and strict particle seeding requirements can be found in Reference 1. The Dual-Plane PIV technique has been around for some time but has seen limited application (Refs. 2 and 3). The author has used both Tomo-PIV and Dual Plane PIV in several different flow fields where extracting all 3-components of vorticity was desired (Refs. 4 and 5). Since these two techniques are capable of providing the same flow field properties through very different routes with significantly different levels of effort, a comparison of their application and performance would prove beneficial in a well-known, 3D flow field. The slightly higher equipment requirements and increased receiver system complexity of the Dual Plane PIV technique can possibly outweigh the strict seeding requirements and massive processing requirements of the Tomo-PIV technique.

Unsteady ejectors have been of continued interest in recent years, due to their similarity to pulse detonation-based propulsion systems, which produce unsteady, impulsive thrust. It has been demonstrated that properly dimensioned ejectors, driven by unsteady thrust sources, often produce higher levels of thrust augmentation, at a considerably smaller size than do those driven by steady jets (Ref. 6). PIV has been previously used at NASA GRC to characterize the thrust augmentation levels achievable in unsteady jets (Ref. 7). Hence, the availability of the synthetic jet hardware and the highly 3D nature of the ejector flow field made it a desirable test bed for assessing the performance of these different PIV measurement techniques.

Synthetic Jets

A synthetic jet can be made from any enclosed chamber with a movable diaphragm and an exit port. As the diaphragm is compressed, decreasing the volume of the chamber, a pulse of fluid is ejected from the chamber that rolls up into a classic toroidal starting vortex as it shears with the ambient air. The starting vortex continues to ascend above the synthetic jet exit plane as the intake phase begins when the diaphragm retracts, decreasing the volume of the chamber, drawing air back into the chamber. This cyclical intake/exhaust process continues at the driving frequency of the diaphragm. A simple schematic layout of a synthetic jet is shown in Figure 1. A more detailed description of prior work using this particular synthetic jet can be found in Reference 7. An 8 in., dual coil speaker was mounted on the back of a sealed cylindrical cavity. The top of the cavity was sealed by a 228×228 mm plate. A 30 mm diameter hole was cut into the top plate creating the exit/entrance port. A multi-I/O board in the data acquisition pc was used to generate a 50 Hz sine wave signal, which was then split and sent to both an audio amplifier and a digital delay generator. The audio amplifier was used to generate the sine wave signal to drive the speaker. The RMS voltage of the amplified sine wave was measured using a digital volt meter (DVM). The sine wave signal was also connected to the external trigger input on a digital delay generator, which generated a 50 Hz TTL signal for every high to low crossing of the sine wave at 1 V. The digital delay generator was used to further reduce the 50 Hz sine wave signal down to a 10 Hz TTL signal in order to trigger the PIV system, thereby phase locking the PIV system to the synthetic jet drive signal. Phase stepping of the PIV system acquisition relative to the synthetic jet cycle was obtained by increasing the time delay from the trigger off of the sine wave to the generation of the 10 Hz TTL PIV trigger signal. Longer time delays capture the toroidal vortex at higher positions above the exit plane, and also reveal the beginning of the intake phase of the cycle.

The synthetic jet assembly was placed on its own translation stage inside a five sided glass chamber which measured 90×45×45 cm (H×W×D), see Figure 2. The translation stage was used to move the exit plane of the synthetic jet relative to the fixed light sheet location of the PIV systems. The large chamber yielded an *L/D* ratio of 30 in the vertical axis and *L/D* of 15 in the horizontal plane, which should allow adequate space to minimize any boundary effects on the flow. For all of the PIV experiments reported here, the synthetic jet was operated at 50 Hz, 4.6 V RMS. A black plate was placed on the open side of the chamber to seal off the charge of flow seeding material and to provide a black background for the PIV imaging cameras.
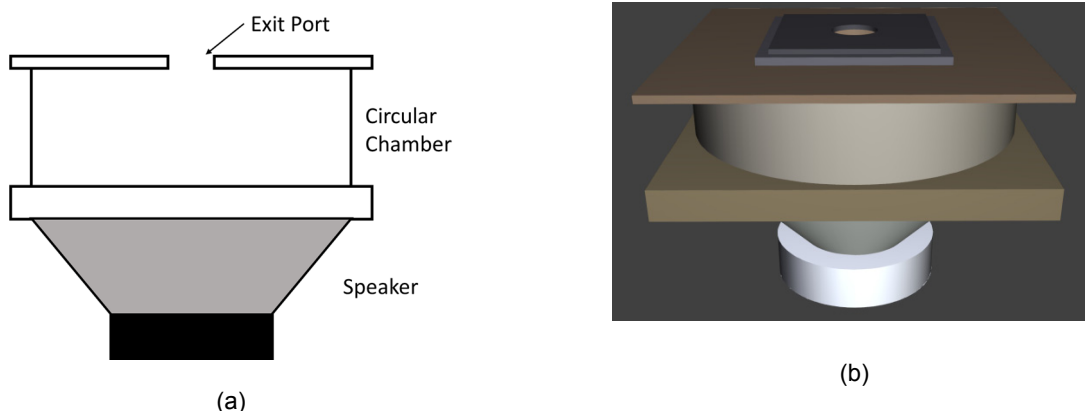

(a)

(b)

Figure 1.—(a) Schematic diagram of a synthetic jet, (b) CAD model rendering of the synthetic jet. A speaker is attached to the bottom side of a circular chamber with a small exit port on the top of the chamber. All flow enters and exits through the single port in the top plate.
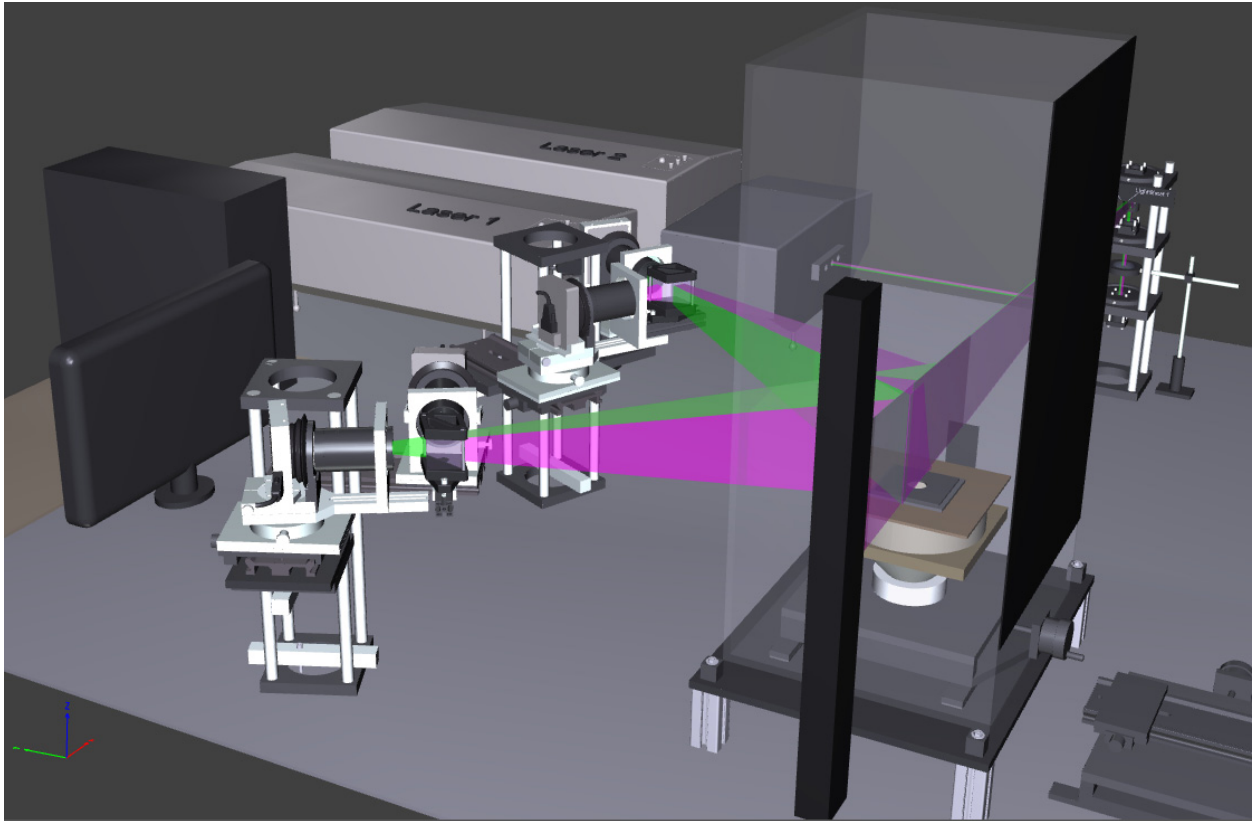
Figure 2.—CAD rendering of the Dual-Plane PIV setup showing the synthetic jet mounted inside the glass chamber on top of a translation stage. The polarization of the light sheets is coded by color. The polarization beamsplitting cubes separate the light from the respective laser light sheets to the proper camera. The two laser heads used to generate the two parallel light sheets in the flow are shown in the background.

Three PIV Techniques Applied to the Synthetic Jet

The basic Particle Image Velocimetry (PIV) technique is relatively easy to setup and provides accurate measurements (~1 percent of full scale) of the flow field velocity across an extended planar domain. In PIV, a pulsed laser beam is formed into a thin sheet which is used to illuminate small particles entrained in a fluid at two closely spaced instants in time. The positions of the particles in the fluid are recorded on special "frame-straddling" high resolution electronic cameras. Cross-correlation processing of the image pair across a grid of subdivided regions enables computation of the flow field velocity across the illuminated plane. Since PIV measures the motion of the particles instead of the fluid or gas itself, it is imperative that the seed particle size and material be judiciously selected in order to insure that the particles are able to faithfully follow the flow.

There are several different implementations of the PIV technique where additional hardware, setup and calibration are required in order to extract more fluid mechanical properties of the flow. The four most common implementations of the technique are: (1) standard two-component (2C) PIV; (2) Stereo PIV (SPIV); (3) Dual Plane PIV; and (4) tomographic PIV. The 2C PIV technique provides 2-componet measurements across the illumination plane and has the smallest optical access requirements. SPIV provides 3-component velocity measurements across a single plane. Dual Plane PIV and Tomo-PIV provide 3-component velocity measurements across two or more planes, which then enables the computation of cross-plane flow field properties. The details of implementing SPIV, Dual Plane PIV and Tomo-PIV, which were all used in this investigation, are described next.

Stereo PIV

Stereo PIV is an extension of the traditional 2C PIV technique where a pair of cameras are oriented in a left/right stereo viewing configuration to record two different views of the particles illuminated in a thin laser light sheet, see Figure 3. The object plane in Figure 3 also represents the thin laser sheet plane. Due to the tilted object plane relative to the left and right camera views, the Scheimpflug condition is used to insure all points are in focus on the CCD sensor plane, which requires that the plane of the camera sensor be tilted relative to the camera lens. When the plane of the laser light sheet, the plane through the center of the lens and the plane through the face of the sensor all intersect at a common point, the Scheimpflug condition is satisfied and all points on the sensor remain in focus across the obliquely viewed object plane (Ref. 8). Each acquired image pair from the left and right cameras are cross-correlation processed in order to obtain the 2-component velocity vector maps. The vertical displacements are redundant in the left and right vector maps. The 3-component red vector, shown sticking out of the object plane in Figure 3, appears to be of different lengths in the left and right camera views projected onto the object plane. This apparent difference in the horizontal velocity components is indicative of the out-of-plane velocity component and is used to reconstruct the 3-component velocity vector using standard PIV algorithms. Hence, by using two cameras, SPIV provides all three components of velocity across a single measurement plane. However, only the in-plane vorticity component ω_z can be computed from SPIV data sets.

A single computer system equipped with a NASA GRC in-house code called PIVACQ was used to control all of the different PIV systems employed in this synthetic jet experiment. Since PIVACQ is an in-house code it can be easily modified to support changes in the experimental hardware configuration for these various PIV system implementations. Additionally, for all of the PIV system implementations, 4008×2672 pixel cameras were used. For the SPIV configuration, the pair of PIV cameras were mounted in portrait mode and equipped with 130 mm lenses and 14 mm extension tubes in order to achieve a nominal 128×158 mm reconstructed field of view. The cameras used in the SPIV setup were controlled by a single computer system equipped with a framegrabber board connected to a camera control unit and streamed to disk in real-time.
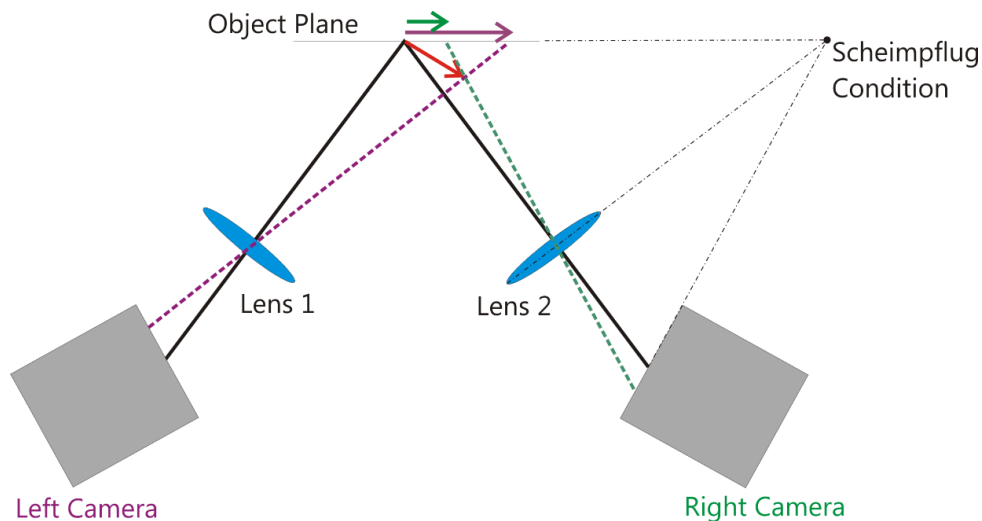

Figure 3.—Stereo PIV system schematic illustrating the Scheimpflug configuration of the camera, lens and object plane in order to keep all points in focus across the object plane. The left camera and right cameras each see the 3D vector projected onto the object plane as different lengths, due to their different viewing directions. The difference in the apparent vector length is used to compute the out-of-plane velocity component.

The SPIV system was calibrated using a dot grid calibration target, which was mounted on a translation stage inside of the synthetic jet glass chamber. A single calibration was used since the optical system was not moved relative to the center of the synthetic jet. The calibration target was aligned with the laser light sheets and then translated to five different planes in 0.5 mm increments spanning the 1 mm z-axis extent of the light sheet. In addition to performing calibrations to a 3rd order polynomial, a calibration verification operation was performed to ensure that the calibration plane was accurately aligned with the plane of the laser light sheet (Ref. 9).

In order to obtain the initial 2-component velocity vector maps, the acquired SPIV image pairs are processed using multipass correlations with 64×64 pixel subregions on 32 pixel centers, followed by 32×32 pixel subregions on 16 pixels centers. Subregion distortion processing is also used to minimize the effects of any velocity gradients across the subregion and minimizes the "peak-locking" effect (Ref. 10). In the subregion distortion technique, the local velocity gradients surrounding the current correlation subregion are used to distort the subregion before the cross-correlation processing operation. Distorting the subregion in this manner yields correlation subregions with uniform particle displacements, and hence, reduces any bias caused by the velocity gradients. Typically two additional passes after the multi-pass processing are used with subregion distortion applied to refine the correlation peak estimates. The Left and Right vector maps are then processed using an in-house code to compute the 3-component velocity vector maps. Sequences of 200 velocity vector maps were acquired at each measurement station and ensemble averaged to provide first and second order statistics over the entire measurement plane. Chauvenet's criteria was used to eliminate any outliers in the ensemble averaging process (Ref. 11). The final processed grid of SPIV data had an in-plane resolution of 0.75 mm

Dual-Plane PIV

Dual-Plane PIV consists of making two sets of planar 3-component measurements in a flow in order to compute the cross-plane flow field properties. Two SPIV systems are focused on two separate, parallel light sheet planes which are closely spaced in the flow (Refs. 2 and 3). A pair of dual-head, pulsed PIV type lasers are required in order to provide the proper parallel plane light sheet illumination. Polarization separation is used to isolate the scattered light from the two SPIV systems since the 1st and 2nd exposures for both SPIV systems are occurring simultaneously. The SPIV cameras image the orthogonally polarized light sheets through 50 mm polarizing beam splitting cubes in order isolate the two optical systems, see Figure 4. The SPIV cameras are mounted in Scheimpflug type mounts in a portrait orientation and are oriented at ±38° to the plane of the laser light sheet. Stereo PIV system #1 uses a dual head laser which has *p*-polarized light straight from the laser, which is vertically polarized in the plane of the laser sheet in the test chamber. Stereo system #1's cameras view the reflected light from the polarizing beamsplitting cube and are oriented at right angles to the observation direction. Laser system #2 uses a half wave plate to rotate the polarization of both laser pulses into *s*-polarized light which is horizontally polarized in the test chamber (parallel to the plane of the table). The horizontally polarized light sheet was offset 0.75 mm further away from the cameras than the vertically polarized light sheet. SPIV subsystem #2 views the horizontally polarized light from the laser sheet straight through the beamsplitting cube. Hence, although the laser light sheets are nominally 0.75 mm apart, each SPIV system can only detect the light from its respective pulsed laser head. Maintaining good separation of the polarized light places strict requirements on the size of the seed particles used in the flow. Submicron sized seed particles are required in order to avoid depolarization of the scattered light from the particles.
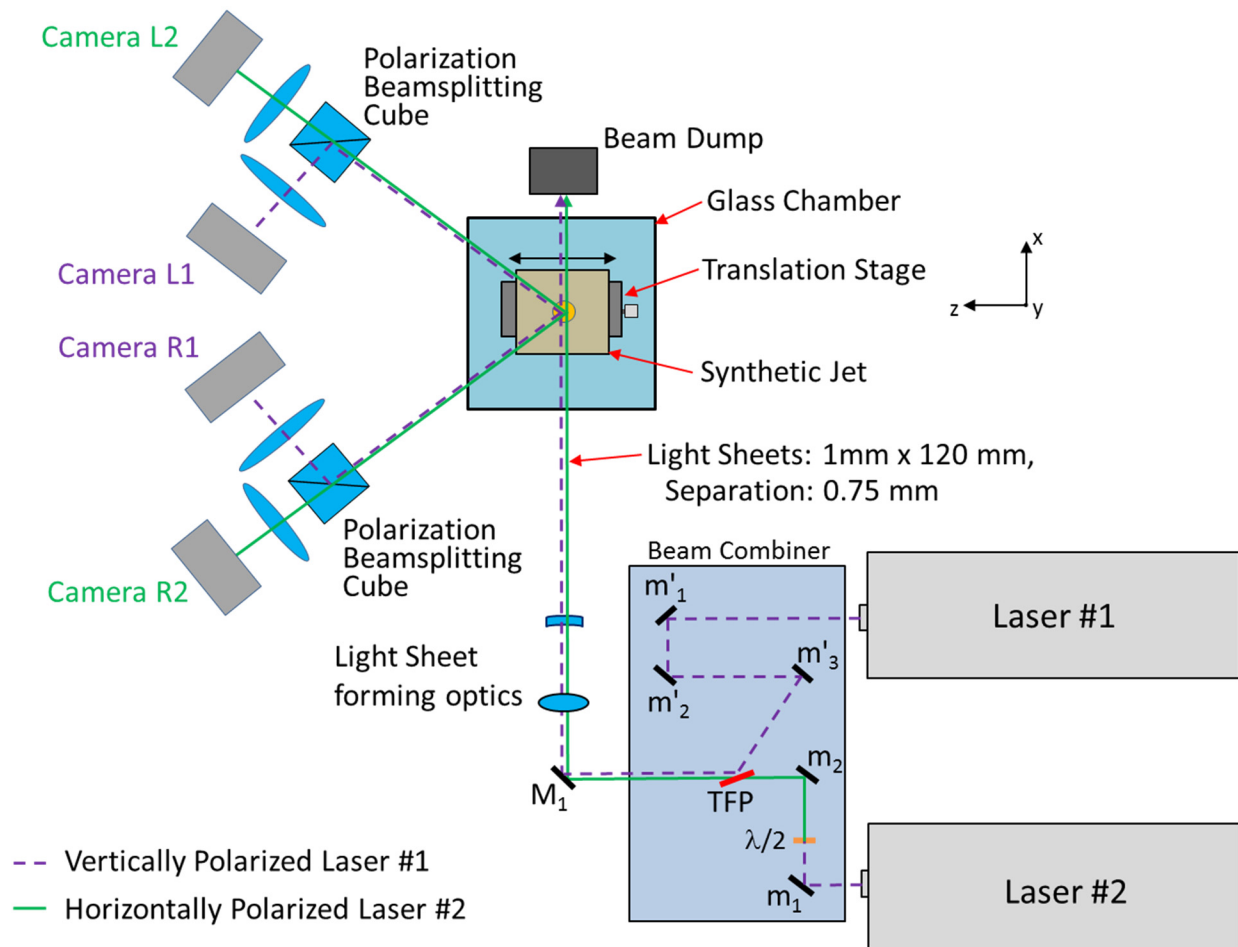
Figure 4.—Schematic layout of laser sheet polarization, beam combining module and Dual Plane PIV receiver system. Both lasers output at 532 nm. The purple colored, dashed laser beam is used to delineate the vertically polarized beam paths, compared to the horizontally polarized solid green beam. The vertically polarized light is reflected by the beamsplitting cube and the horizontally polarized light passes straight through the cube.

The light from the two different dual head laser systems are combined using a beam combiner module as shown in Figure 4. The Nd:YAG lasers used in this work had pulse energies of 400 mJ at a 10 Hz repetition rate. The s-polarized light from laser #2 passed straight through a thin film polarizer (TFP) in the beam combiner. The p-polarized light reflects off of the TFP at Brewster's angle to provide two nearly parallel beams. A slight angular misalignment between the beams is required in order to obtain two closely spaced, parallel light sheets above the exit port of the synthetic jet. The laser beams pass through a –25 mm cylindrical and a 1.5 m spherical lenses to yield a pair of 1 mm thick parallel light sheets that are 150 mm tall and spaced 0.75 mm apart in the test chamber. The light sheets exit the glass test chamber through the back wall and are directed into a beam dump in order to minimize flare light.

In the Dual Plane PIV setup shown in Figure 4, the 4008×2672 pixel PIV cameras were equipped with 130 mm lenses and 14 mm extension tubes in order to achieve a nominal 124×157 mm field of view. All four cameras used in the Dual-Plane setup were controlled by a single computer system equipped with two framegrabber boards connected to two camera control units and streamed to disk in real-time. Both of the laser systems were triggered at the same time so image acquisitions from the two stereo PIV systems were synchronized. Simultaneous acquisition of the flow properties at the two illuminated planes in the flow is required in order to compute the cross-plane flow properties. Image sequences of 200 image pairs were acquired for each measurement station.

The two independent SPIV systems were calibrated using a dot grid calibration target, which was mounted on a translation stage inside of the synthetic jet glass chamber. A single calibration was used since the optical system was not moved relative to the center of the synthetic jet. The calibration target was aligned with the laser light sheets and then translated to nine different planes in 0.5 mm increments spanning the 3 mm z-axis extent of the two parallel light sheets. In addition to performing calibrations to a 3rd order polynomial, a calibration verification operation was performed to ensure that the calibration plane was accurately aligned with the plane of the laser light sheet (Ref. 9).

The Dual Plane PIV image data were cross-correlation processed and ensemble averaged as described in the SPIV section above. The ensemble averaging step was the point at which the data from the two laser light sheets were used to compute the cross-plane flow vorticity, which is the unique aspect of the Dual-Plane configuration. Vorticity was computed on each instantaneous velocity vector map and then the instantaneous vorticity was ensemble averaged to yield the final vorticity estimates. Although two measurement planes were acquired, the data written out were only for a single plane, including the out-of-plane vorticity component estimates. The final processed Dual Plane PIV velocity vector maps had a Dual-Plane spatial resolution of 0.75×0.75×0.75 mm.

Tomo-PIV

Tomo-PIV is a relatively new modification of the traditional SPIV technique where instead of using a thin laser sheet, the positions of particles across a thick laser sheet (volume) are recorded on four or more cameras. Tomographic backprojection techniques are then applied to reconstruct the 3D particle field from the limited number of camera views. The final step in the processing is to perform 3D cross-correlations on the 3D particle reconstruction domains yielding a 3-component mapping of the flow across multiple planes. The number of planes is typically very high since the voxels are uniform cubes, and the spacing between adjacent z-planes is the same as the spacing between x-y-plane subregions. The multiplane data set can then be used to compute both in-plane and cross-plane fluid properties, hence the attraction of the technique.

Tomo-PIV benefits from the large body of work developed and applied in medical imaging systems, where tomographic reconstruction algorithms are used on a daily basis. Commercial tomographic medical imaging systems acquire several hundred images spanning 180° in order to provide high resolution images of human skeletal or organ details. These systems operate with the advantage of a single detector which rotates about a stationary phantom. However, in order to obtain a tomographic reconstruction of a dynamic phantom (such as a fluid flow), all of the views must be acquired simultaneously, which necessitates simultaneous image capture from multiple cameras. Reducing the number of views from several hundred down to six or four views drastically impacts the fidelity of the reconstructions. Limited view reconstructions always yield poor resolution phantoms and artifacts from the backprojections (Ref. 12).

The most common and frequently applied tomographic reconstruction technique used in Tomo-PIV applications is the Multiplicative Algebraic Reconstruction Technique (MART) and the modifications of the MART (Refs. 1, 13, and 14). These algebraic reconstruction techniques are most suitable to the limited number of views and type of image data contained in PIV images. The commonly accepted approach is to preprocess the particle images to maximize the SNR in the images by applying local average thresholding, Min/Max filtering techniques and optionally, 3×3 Gaussian low pass filtering. Multiple iterations of the MART algorithm are typically applied to the preprocessed images, where five iterations is the most commonly cited value. These backprojection techniques are able to generate moderate fidelity reconstructions of the particle field when the particle concentration is low. However, as the particle concentration increases, the reconstruction domain becomes increasingly contaminated with "ghost" particles and well defined, spherical, discrete particle shapes are seldom observed. Instead, a complex grid of intersecting projections is observed, sometimes leading to bright particles above the noise of intersecting lines (particle projections through the reconstruction domain). All of the reconstructed
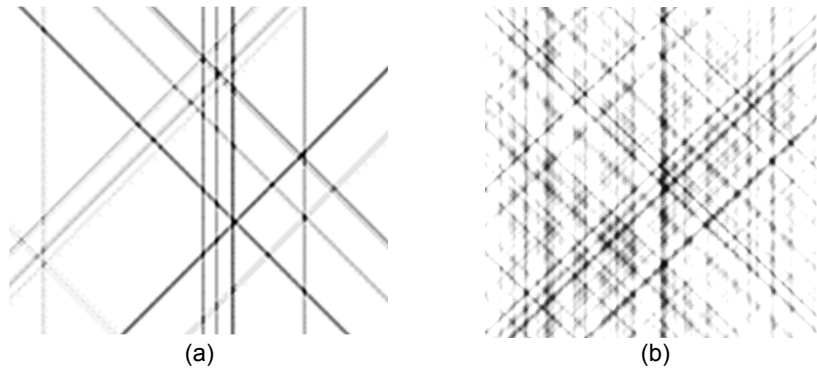
Figure 5.—Sample slice through a backprojection reconstruction domain, where the gray scale has been inverted: (a) low particle concentration, (b) high seed particle concentration. The ghost particles are all of the non-white gray regions and the actual reconstructed particles are the black regions. The projections of the recorded particle images from each CCD array through the domain yield the cross hatching pattern. Applying more camera views decreases the amount of cross-hatching in the reconstruction.

shapes are essentially parallelograms, due to the nature of the back projections. An example of a backprojected reconstruction is shown in Figure 5 where an inverse gray scale is used to accentuate the particle intensities. Ghost particles are formed when less than the total number of camera projections intersect at a point. All of the intersecting projections that do not yield a bright particle (black regions in the figure) are actually ghost particles (all of the gray regions). Ghost particles reduce the SNR and cause false correlation difficulties in the 3D cross-correlation processing.

As mentioned above, preprocessing the raw images to increase the SNR is standard practice in Tomo-PIV. Many researchers also elect to apply a 3×3 filter to the raw image data, in order to compensate for misalignment of the cameras. Misalignment of the cameras adversely affects the quality/existence of the projected particle reconstructions, hence the 3×3 filter blurs out the particle images to aid in the overlap of the back projections. Normally in PIV, the goal is to minimize the size of the correlation peak in order to maximize the accuracy of the estimated particle displacements (Ref. 15). Applying a 3×3 filter to the raw image data smears out the particle images which leads to a degradation in the accuracy of estimating the 3D cross-correlation spheroid.

Nominal ±45° camera viewing angles yield reconstructed particles that are 40 percent longer than their width, which produces smeared out correlation spheroids in the 3D cross-correlation computations. The only way to reconstruct accurate particle shapes with minimal ghost particles is to acquire several hundred independent views spanning 180°. Increasing the number of views (adding more cameras) is critical to improving the reconstruction quality. Typically, not enough emphasis is placed on the desirability/necessity of using more camera views in performing the Tomo-PIV technique. Unfortunately, this guidance is ignored in the present work due to the limited number of high resolution cameras available for the test.

The camera layout/configuration also plays a significant role in the ultimate resolution and quality of the tomographic reconstructions. The goal is to maximize the useable area of each camera sensor and its overlap with the views from all other cameras in the system. While three cameras are the absolute minimum, 4-camera tomographic configurations are the most common (Refs. 1, 13, and 14). Due to the broad base of the synthetic jet platform relative to the location of the cameras, we chose to implement a Quad camera configuration, where all of the cameras are oriented in the same horizontal plane, at nominal angles of ±17° and ±38°, see Figure 6. Keeping the cameras in the same horizontal plane simplifies the setup of the optical systems and avoids obscuration of the measurement volume by the model hardware. The large range of camera angles helps to reduce the reconstructed size of the particles in the horizontal plane – but there is little refinement of the particle shapes in the vertical axis, since all of the camera views are in the same horizontal plane. Assuming that non-square CCD sensors are being used and that nearly square reconstruction domains are desired, then orienting the camera sensors in portrait mode
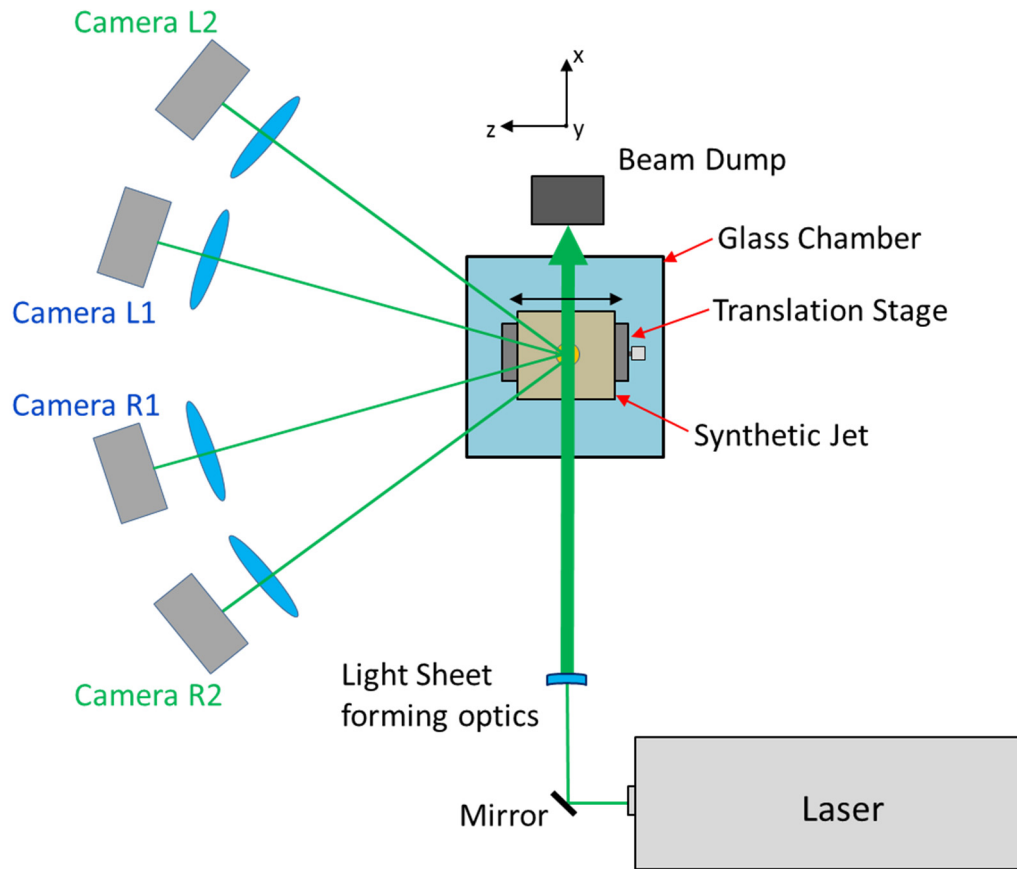
Figure 6.—Schematic overhead layout of the tomographic PIV camera setup where all of the cameras are positioned in same horizontal plane and the thick light sheet passes over the center of the synthetic jet exit port. The Tomo-PIV camera configuration can be viewed as two stereo pairs: camera L1/R1 and cameras L2/R2. The SPIV data was collected using the L2/R2 camera pair and a 1 mm thick light sheet.

(highest pixel count axis oriented vertically) facilitates the most efficient utilization of the camera field of view, since the images are compressed across the Scheimpflug axis of the camera sensor. Upon reconstruction, the foreshortened axis increases in proportion to the camera tilt angle relative to the plane of the light sheet. Hence, if the quad camera system is viewed as two stereo PIV systems (L1/R1 and L2/R2) with different coupling angles, the reconstructed images will never have the same width. The inner pair of cameras L1/R1 will have the smallest reconstruction width and therefore define the dimensions of the tomographic reconstruction volume.

The development and implementation of the Tomo-PIV reconstruction algorithm for the high resolution images acquired in this work presented several challenges regarding computational efficiency, processing memory (RAM) and hard drive storage. The reconstruction volumes were first computed and then stored for subsequent 3D cross-correlation processing. For the high resolution images (4008×3672 pixels) acquired here, the reconstruction algorithm domains were nominally 3950×2700×222 voxels. Precomputing the pixel mapping weights required >200 GB of system RAM, hence the weights were computed on the fly as required and saved when storage permitted. The reconstructed domains required several Terabytes of storage space for a single measurement station. Tests were performed to determine the minimum file storage format to ensure accurate reconstructions could still be obtained. The reconstructed volumes were stored as single byte per pixel binary files. In the 2nd step of the processing, these binary files were then 3D cross-correlation processed to determine the particle displacements. This 2-step approach enabled the optimization of the 3D cross-correlation settings before the reconstruction domains were deleted. Each of the two steps was very computationally intensive.

The Tomo-PIV and SPIV data were collected on the same day using the same camera configuration. All four cameras high-resolution (4008×2672 pixels) cameras were configured, mounted and focused on the light sheet plane, as shown in Figure 6. The cameras were equipped with 130 mm focal length lenses, 14 mm extension tubes and operated at f/8. For the SPIV measurements, only images from the L2/R2 stereo camera pair were used with a 1 mm thick light sheet. For the Tomo-PIV measurements, images from all four cameras were acquired and a light sheet thickness of 10 mm was used. Calibrations were performed using a single plane dot grid target translated to 11 axial positions over a ±5 mm range. A 3rd-order polynomial was used in the calibration and a calibration verification operation was performed on the Tomo-PIV camera system to ensure that all cameras were registered to the common calibration to within 0.1 pixel. As described in the Dual Plane PIV section, all four cameras were connected to a single computer system and 200 frame pair data sequences were acquired and streamed to disk at a rate of 2 frame-pairs/camera/sec.

The raw PIV image data from the four cameras were processed using five iterations of MART reconstruction processing. As stated above, the common practice in Tomo-PIV is to preprocess the raw images before applying the tomographic reconstructions. The effectiveness of these preprocessing steps was evaluated by processing the image data in several ways. First the raw image data was directly processed using the tomographic reconstruction algorithms and velocity fields were extracted from the 3D particle fields with no difficulties. Next, local thresholding and local Min/Max filtering were applied. These preprocessed images yielded very poor quality velocity field results. It was determined that application of the 3×3 Gaussian low pass filtering was required after the local thresholding and local Min/Max filtering in order for velocity fields to be extracted. It appears that the SNR enhancement preprocessing step, necessitates the application of the 3×3 Gaussian low pass filter in order to extract velocity fields. The quality of the velocity fields extracted from the Tomo-PIV image data was the same, with or without image preprocessing. Hence, image preprocessing of Tomo-PIV image data does not appear to be a requirement and was therefore not used in the results presented here, which is in contrast to the requirements reported by others (Ref. 1).

Due to the use of the high resolution cameras in the Quad configuration, a large reconstructed volume (3900×2700×220 voxels) was obtained. The MART reconstructions computed in this work were 3-D cross-correlation processed using a NASA GRC in-house code called pivbatch3D. Pivbatch3D is a Fortran based batch processing code for processing large volumes of Tomo-PIV image data, that performs 3-D cross-correlations in multi-pass, window offset processing and also provides subvolume distortion processing (Ref. 10). Fortunately, the 3D cross-correlation processing is able to identify the larger intensity reconstructed particle "blobs" above the cross-hatching and ghost particle laden background common to all of the moderate to high seed particle concentration Tomo-PIV reconstruction domains. The particle displacements were found using 3-pt Gaussian peak estimators on each axis of the correlation spheroid. Our experience with multi-threaded applications is that the overhead in managing the threads leads to a reduction in the overall computational utilization of all of the CPU cores. Hence, full 100 percent computation efficiency is rarely achieved using multi-threaded code. Pivbatch3D achieves 100 percent computational efficiency by first determining the number of CPU cores available on the host processing platform. Then the program spawns a separate process for each processing core in the CPU. Each process is given a subset of image pairs to correlation process. There is no interdependency on the spawned jobs and each one operates as a separate process, with its own memory and most importantly a single dedicated CPU. True 100 percent utilization of the full CPU capacity is achieved provided sufficient system RAM is available to support all of the spawned processes. The systems used to process the PIV data in this work were dual Xeon, 12 core processors equipped with 192 GB of RAM. With Hyperthreading enabled, 48 cores were available for processing.

The Tomo-PIV reconstructed 3D particle fields were processed using an initial pass of 64^3 voxel subvolumes on a 32^3 voxel grid. A second pass using 32^3 voxel subvolumes on a 16^3 voxel grid (50 percent overlap) was used and then a final pass using the same grid parameters with 3D subvolume distortion processing applied. The final processed 3D domain contained 12 velocity planes with a spatial

resolution of 0.72×0.72×0.72 mm across the 110×170×8.6 mm reconstructed volume. Sequences of 200 velocity vector maps were acquired at each measurement station and ensemble averaged to provide first and second order statistics over the entire measurement plane. Chauvenet's criteria was used to eliminate any outliers in the ensemble averaging process (Ref. 11). In addition to the standard flow field properties obtained using stereo PIV, all three components of vorticity were computed across the volume.

Flow Seeding

As described in the introduction to the PIV technique, it is the velocity of the particles entrained in the flow that is measured, not the gas velocity itself. Hence, the particle size and material must be selected to ensure that the particles will faithfully follow the fluctuations in the flow (Ref. 16). Submicron particles are required for supersonic flows, while larger particles are suitable for less dynamic systems. Generally, for 2C PIV and SPIV, the particle size is dictated by the fluid dynamic properties of the flow field under study. However, the Dual-Plane PIV technique used here placed additional restrictions on the particle size that could be used, even in low speed flows. The Dual Plane PIV technique relies on polarization separation to isolate the optical systems. Hence, a crucial parameter in any optical system relying on polarization isolation is the scattering particle size. If the particles are too large, then the scattered light will be depolarized and both optical systems will see the scattered light from both lasers, thereby cross-contaminating the recorded particle images. Particles less than 1 µm in diameter preserve the polarization state of the incoming light. Hence, there is a strict requirement that the seed particles used in the experiment must be less than 1 µm in diameter.

Tomo-PIV is extremely sensitive to the seed particle concentration across the imaged volume. In standard PIV, a thin slice of the fluid is illuminated and imaged onto the CCD camera and there is typically 5 to 10 pixels between adjacent particles on the image. However, in Tomo-PIV, a thick volume of the fluid is illuminated and imaged onto the CCD. In the setup used here the light sheet was 10x thicker, resulting in an order of magnitude more particles being recorded on the CCD. Hence, for Tomo-PIV the chances of recording overlapping particle images on the CCD is greatly increased. Overlapping particle images further degrades the quality of the reconstructed 3D particle field. The imaged concentration of particles onto the CCD is called the source density N_s, which is equal to the number of particles per pixel (Ref. 1). If the particle overlap exceeds $N_s = 0.5$, the quality of the reconstruction is very poor since there is minimal modulation in the intensity in the recorded images. Hence, in Tomo-PIV the concentration of seed particles must be carefully controlled.

The synthetic jet used in this work was placed inside a large glass chamber while making the PIV measurements. If left open to the free air, it would be difficult to seed both the ambient air and the cyclical plumes of air ejected from the jet. The benefit of a closed chamber is that the recirculating flow field in the synthetic jet can be seeded everywhere, by simply charging the chamber with seed material. A cryogenic freeze spray, similar to commercial spray cans used for dusting off surfaces, provided a good source of seed material, which eventually evaporated, leaving no residue in the chamber. The closed chamber provided a unique environment where the charge of freeze spay provided aerosol droplets in the flow which lasted several minutes. Prior to each image acquisition sequence, the chamber was flooded with the atomized freeze spray. The aerosol formed by the freeze spray generates droplets that quickly evaporate to submicron size. As the aerosol ages the droplets continue to evaporate and therefore decrease in size. The submicron size of the particles was verified by checking the cross-contamination of the Dual Plane PIV system. Neither SPIV viewing system could see the laser light from the adjacent laser sheet, confirming the two optical systems were isolated and that the particles were submicron in size. Freeze spray seeding was used for all of the different PIV measurements reported here.

In Tomo-PIV the recorded particle image concentration has a significant impact on the quality of the reconstructed 3D particle fields. The recorded particle images obtained in this work contained particles on the order of 2 pixels. The number of particles per pixel (*ppp*) was estimated using a centroid finding program which analyzed small 128×128 subregions of the image. The average source density is estimated to be around *ppp* = 0.045.

Measurement Error

The recording and subsequent reconstruction of 3D particle fields required in Tomo-PIV is a very complicated and tedious process with the potential for many error sources in each step of the process. Three-dimensional particle field generation and optical imaging system simulations were used to develop and access the accuracy of the reconstruction techniques used in this work. As in any simulation, not all of the error sources are typically known and/or modelled correctly to match the real world experiments. Hence, the simulations only provide a rough sense of the errors that will be realized in such a complicated multi-step flow measurement technique. The approach assumed in this work is to employ the well characterized SPIV technique as the defacto standard by which the Tomo-PIV measurements are compared. Both the standard SPIV and Dual Plane PIV provide equal standards for evaluating the Tomo-PIV results.

Barring any significant bias errors, the measurement errors for standard SPIV are essentially determined by how accurately the cross-correlation peak centroid can be measured. The relatively low velocity flows (< 20 m/s) in the synthetic jet were seeded with the submicron particles which will faithfully follow the flow, hence, velocity lag is not a significant error source. Subregion distortion processing is used to mitigate any effects from velocity gradients across the measurement subregions and avoid "peak locking" (Ref. 10). For the SPIV optical system configuration, the particle displacements were nominally 10 pixels in the synthetic jet core and the correlation peaks were measured to 0.1 pixel accuracy. Hence, the in-plane displacement error in the SPIV measurements is < 1 percent of full scale. The out-of-plane SPIV error is inversely proportional to the tangent of the coupling half-angle between the cameras. Since the SPIV cameras were configured at ±38° to the jet axis, the error in the out-of-plane x-component displacements is 1.3 times the in-plane error, which is still on the order of 1 percent of full scale. Ensemble averaging 200 measurements yields mean flow statistics below 1 percent of full scale for the SPIV measurements.

Results and Discussion

The synthetic jet was placed inside the glass chamber and SPIV, Dual Plane PIV and Tomo-PIV measurements of the synthetic jet flow were acquired. The coordinate system for the data sets are centered at the synthetic jet exit port center, where the laser light sheets are oriented in the x-y plane and the synthetic jet was traversed in the z-direction. Due to the symmetry of the pulsed jet flow field only one half plane of the flow was measured. The PIV systems were phase locked to the driving frequency of the synthetic jet. Hence, data sequences were acquired across a range of phase steps spanning the 20 ms cycle time of the synthetic jet periodic flow. Tomo-PIV data were collected with a 10 mm thick sheet, at three locations from the nozzle centerline: Z = 0, 10, and 20 mm. SPIV data were collected using a 1 mm thick light sheet and the light sheet was traversed to z-planes of 0, 2, 4, 6, 8, 10, 14, 18, 22 mm. Dual Plane PIV data were collected using two orthogonally polarized 1 mm thick light sheets, spaced 0.75 mm apart that were traversed over the range of 0 to 22 mm in 2 mm increments.

The stereo PIV data and the Tomo-PIV data were collected on the same day, while the Dual Plane PIV data were collected several months later when it was determined that a comparison data set would be beneficial in evaluating the Tomo-PIV data. The phase stepping between the two experiments, although initially believed to be identical, was actually slightly different. Results from two different plume heights above the exit plane of the synthetic jet are presented: vortex core heights of 35 and 80 mm. There is nominally a 5 mm difference in the height of the vortex plumes between the Dual Plane data and the SPIV and Tomo-PIV data. The SPIV data are considered the benchmark for any in-plane measurements. Dual Plane PIV, based to two simultaneous, and closely spaced stereo PIV measurements is considered the benchmark for the cross-plane measurements. In most aspects all three of the data sets appear to be identical, however; in several aspects there were significant differences revealed between the thin sheet and thick sheet techniques.

The SPIV, Dual Plane PIV and Tomo-PIV reconstructed plumes from the synthetic jet are shown in Figure 7 where the plume height is 35 mm above the synthetic jet model, which is shown in the figure for reference. Contours of velocity magnitude are used in each of the plots and all of the data sets are scaled to the same range. The ambient fluid flow has been blanked by restricting the regions of the data plotted to be > 2 m/s. The Dual Plane PIV data set has 13 planes spaced at 2 mm intervals across the z-axis, which is a fairly high resolution data set. The SPIV data are nearly identical to the Dual Plane PIV data, with a slightly larger plane spacing at the outermost 3 planes. Both of the thin sheet processed data sets have a spatial resolution of 0.74×0.74 mm, and the Dual Plane technique has an added z-plane resolution of 0.75 mm. The Tomo-PIV data set has nearly three times the number of measurement planes than either of the thin sheet PIV data sets. When the Tomo-PIV image data were acquired it was assumed that the reconstructed data sets would span the full thickness of the laser light sheet used to illuminate the flow, hence a 10 mm step size between data planes was used. However, the reconstructed domains are slightly smaller than the 10 mm thick light sheet. Within each of the three reconstructed volumes, the Tomo-PIV
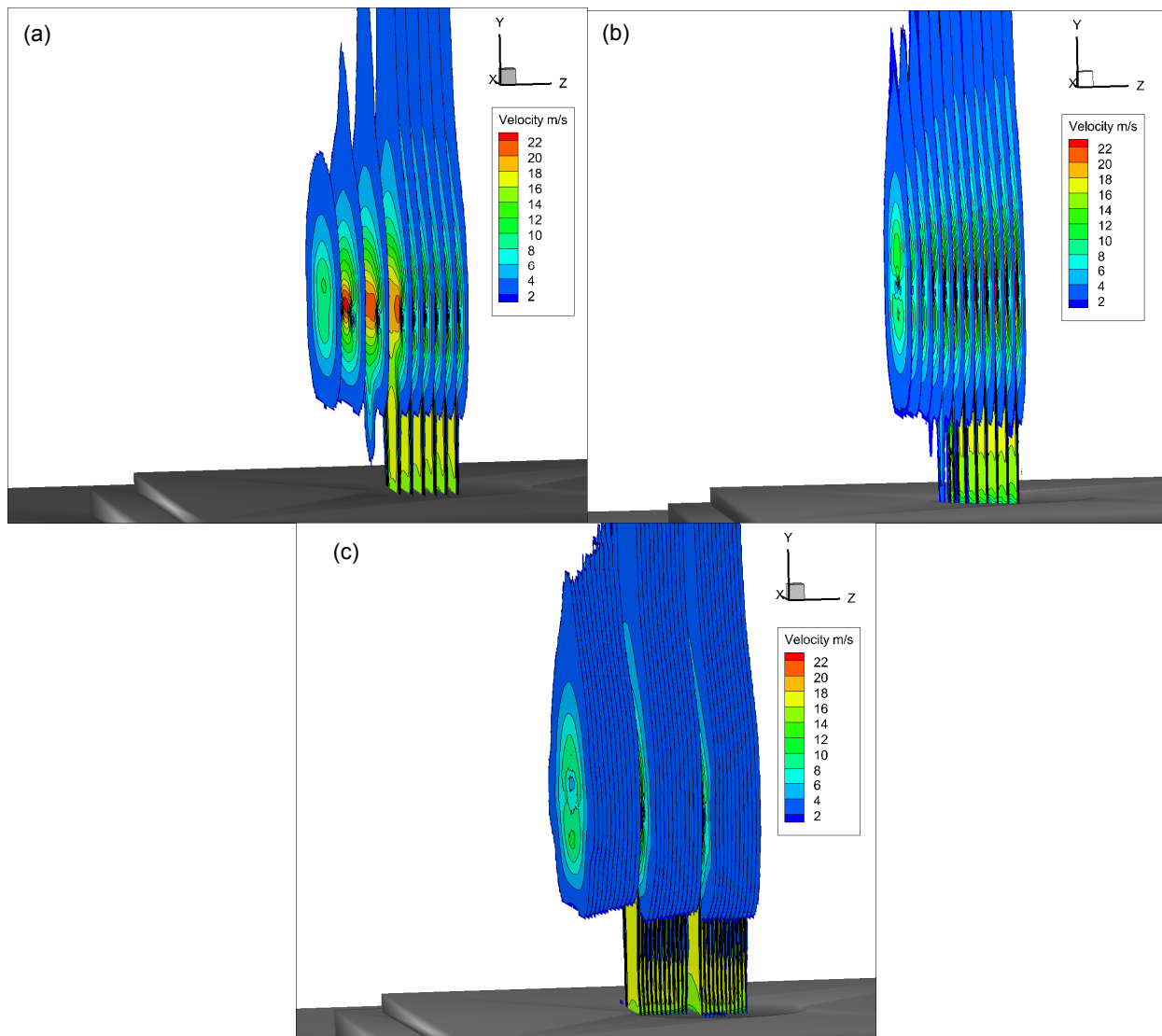

Figure 7.—Contour plots of velocity magnitude of the jet plume at a vortex height of 35 mm above the synthetic jet exit plane for (a) SPIV, (b) Dual Plane PIV, and (c) Tomo-PIV. The Tomo-PIV data set has the highest information density; however, there are slight gaps between the reconstruction domains since the full 10 mm depth of the light sheet plane was not reconstructed.
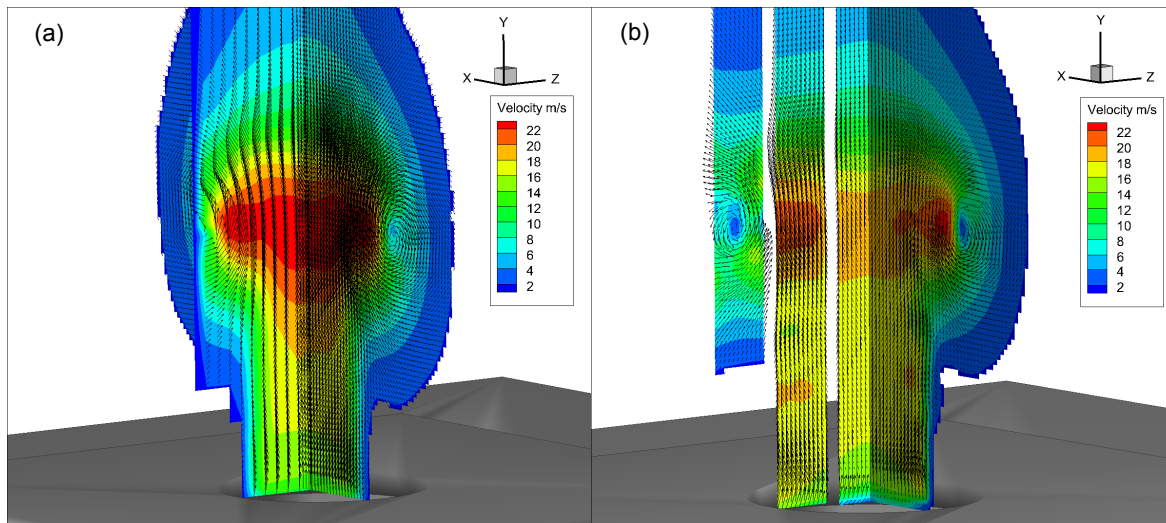
Figure 8.—Orthogonal cutaway view of the 35 mm plume height jet plume core for: (a) Dual Plane PIV and (b) Tomo-PIV data sets. The Dual Plane PIV out-of-plane velocity field slice matches the in-plane flow, a requirement for a rotationally symmetric flow field.

data grid spacing is 0.72 mm in all three coordinate directions and there are 12 z-planes of data spanning 8.6 mm. Hence there are small 2.1 mm gaps between the reconstruction volumes, or just under two missing z-planes. The information density in the Tomo-PIV data sets is much higher than the thin sheet techniques, since the reconstruction grid resolution is uniform in all three coordinate directions. A cutaway view of the Dual Plane PIV and Tomo-PIV data sets at a plume height of 35 mm are shown in Figure 8. Contours of velocity magnitude along with velocity vectors are used to illustrate the flow field. The expected rotational symmetry of the jet plume data are clearly apparent in both of the data sets. The Tomo-PIV data cover a larger extent along the z-axis so that the core of the vortex is fully captured. For the Dual Plane PIV data set, the range of the data collected along the z-axis should have been longer in order to capture the complete extent of the toroidal vortex plume exhausted from the synthetic jet.

The synthetic jet flow has a wide range of complex flow features across the full exhaust/intake cycle. The data shown in Figure 7 is early in the cycle of the synthetic jet and only shows the exhausting plume. Later in the cycle, air is reingested back into the speaker chamber to provide the flow for the next exhaust cycle. The Dual Plane PIV result for the plume height of 80 mm is shown in Figure 9, where again contours of velocity magnitude are shown in an orthogonal plane cut-away view. Here, the jet plume is much higher above the exit plane but the toroidal vortex has not lost any of its strength and is still tightly packed. The intake air is observed to be uniformly drawn circumferentially into the port on the top of the plate.

The reingestion of the air back into the speaker chamber causes an interesting and complex saddle point in the flow. The high speed exhaust plume expelled from the jet decreases in speed as it continues to ascend above the jet and new air is drawn back into the chamber by the receding speaker cone. A detailed vector map comparing the fidelity of the Dual Plane PIV result and the Tomo-PIV result is shown in Figure 10. The SPIV data is not shown since it is identical to the Dual Plane PIV data for this case. The vector maps clearly show the inflection point between the flow exiting the synthetic jet and the new air intake cycle is beginning. A near zero point in velocity is observed between these two opposed flows. The degree of agreement between the two techniques is impressive in this unique flow feature in the synthetic jet flow cycle. There appears to be no measurement error between the Tomo-PIV and Dual Plane PIV techniques in this region of the flow.

At this point in the comparison all three of the data sets agree very well. Comparisons of total turbulence between all of the techniques show a similar agreement. The three measurement techniques appear to be nearly identical when looking at the velocity magnitude and size and shape of the main flow features. However, upon closer inspection the data reveals some discrepancies between the Tomo-PIV data and the two thin sheet PIV techniques.
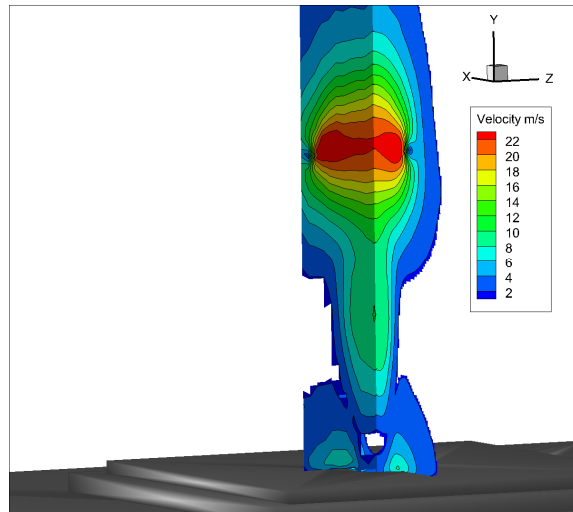
Figure 9.—Another orthogonal cut-away view of the Dual Plane PIV measurements later in the synthetic jet cycle where air is being reingested back into the speaker chamber as the high speed plume continues to ascend.
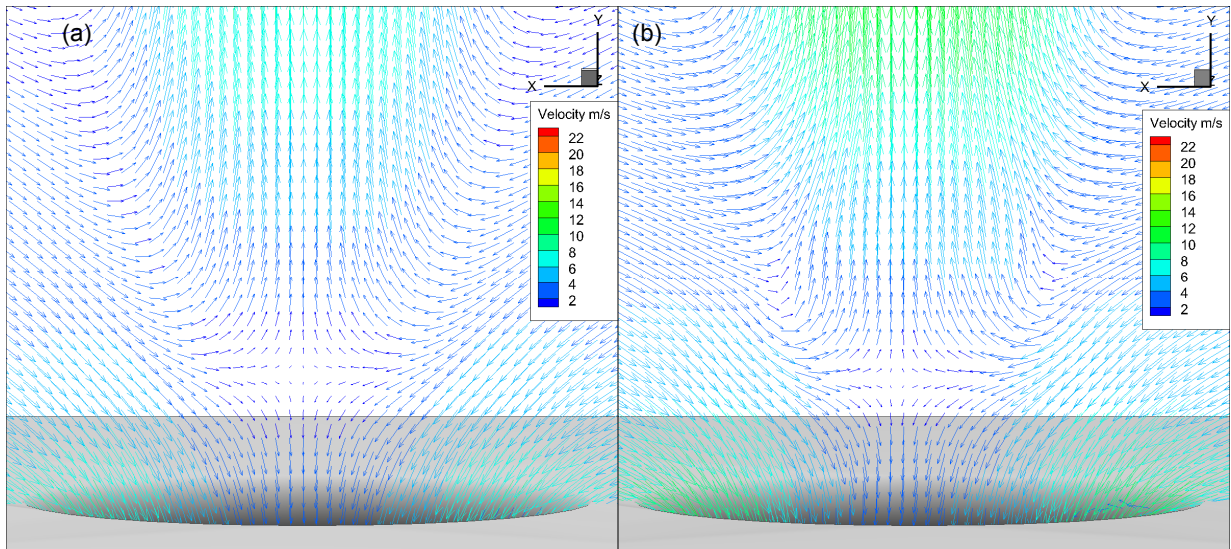

Figure 10.—(a) Dual Plane PIV; (b) Tomo-PIV: Velocity vector maps at z = 0 near the synthetic jet exhaust port during the reingestion portion of the cycle. A saddle point is observed in the flow defining border between the air which continues to move upward with the exhausted plume and the air being reingested into the speaker chamber for the next exhaust cycle.

The first discrepancy found in the Tomo-PIV data is the magnitude of the in-plane vorticity ω_z. Figures 11(a) to (c) shows the computed vorticity for all three measurement techniques at a vortex height of 35 mm above the exit plane. The location and separation between the counter-rotating vortex cores is identical in all three of the data plots. The velocity vector maps also appear to be nearly identical. However, there is an extreme difference in the strength of the vorticity, ω_z. Both the SPIV and Dual Plane PIV vorticity plots show a strong vortex strength with a rotation speed of $> \pm 8000$ 1/s, which is expected from the high velocity jet plume shearing with the quiescent air. Conversely, the Tomo-PIV shows a very mild vortex strength of only ± 300 1/s. The Tomo-PIV vorticity estimate is more than an order of magnitude lower than the SPIV and Dual Plane PIV vorticity maps. This difference in magnitudes persists throughout the entire data set for earlier and later points in the synthetic jet flow cycle. As an additional check on the Tomo-PIV 3D cross-correlation processing, the data were processed without subregion distortion processing and there was no change in the magnitude of the computed vorticity field.
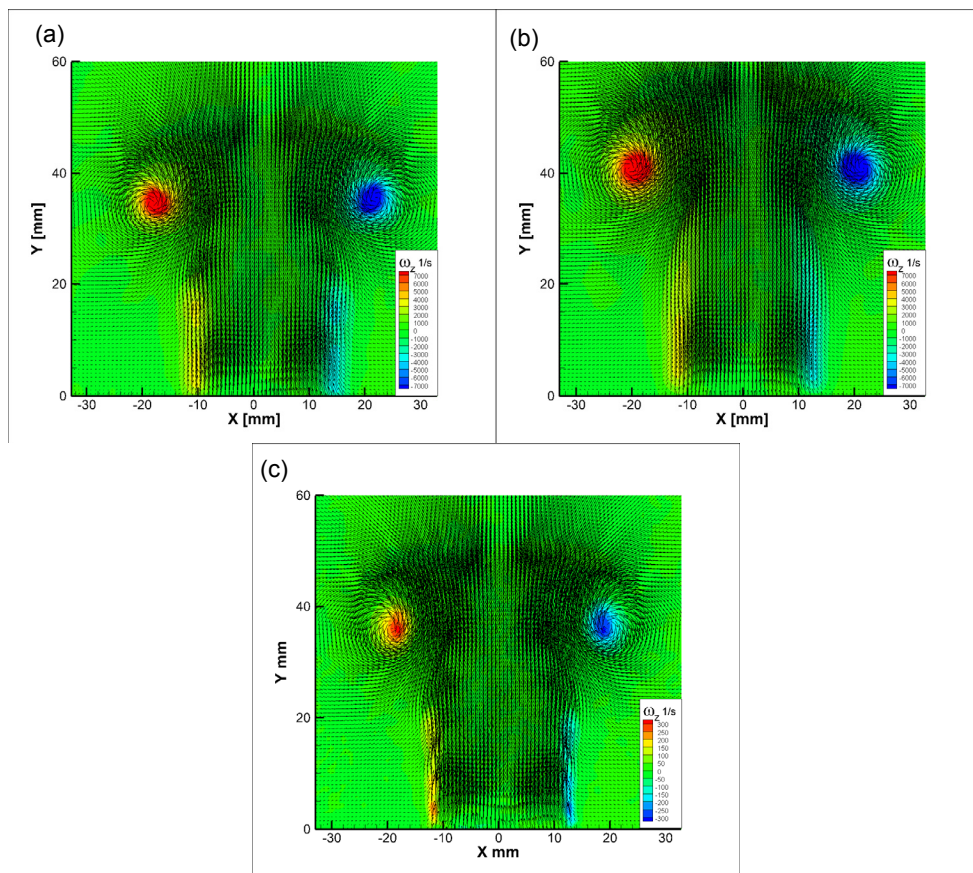

Figure 11.—(a) SPIV, (b) Dual Plane PIV, and (c) Tomo-PIV contour maps of the in-the-plane of the laser sheet vorticity ω_z. The velocity vectors are also overdrawn on the contours. The SPIV and Dual Plane PIV results agree very well with a vorticity of $> \pm 8000$ 1/s. The Tomo-PIV map shows a peak vorticity of only ± 300 1/s.
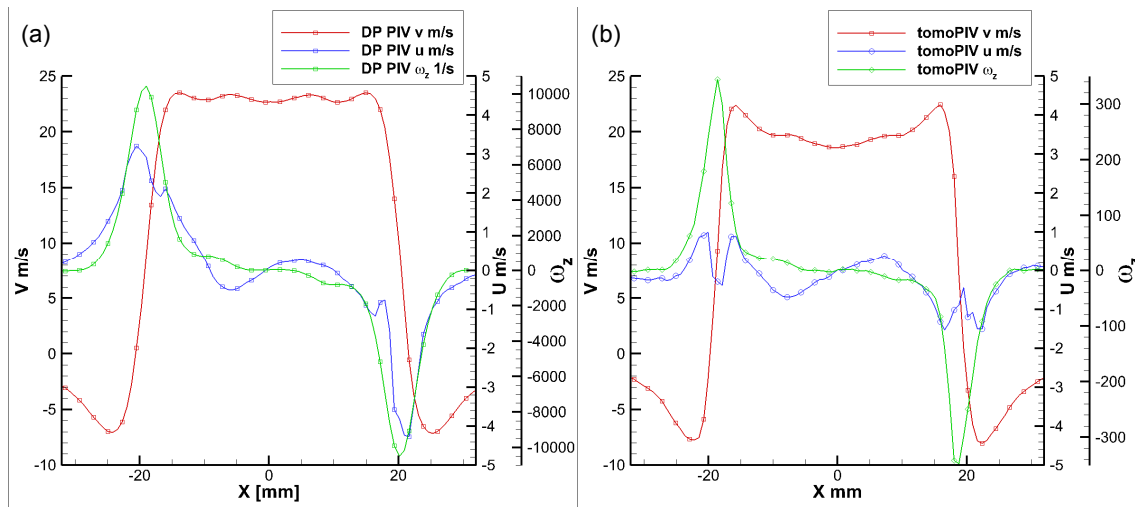
Figure 12.—Line plots of centerline u- and v-components of velocity along with vorticity for (a) Dual Plane PIV and (b) Tomo-PIV. Tomo-PIV did not measure the u-component of velocity, resulting in the gross under estimation of the vorticity ω_z.

The low estimate of the z-component of vorticity obtained from Tomo-PIV is disturbing. The SPIV and Dual Plane PIV both agree in the level of ω_z of ±11000 1/s. The main error observed is in the computation of the vorticity in the Tomo-PIV data. Figure 12 shows line plots through the horizontal vortex centerlines for the Dual Plane, Figure 12(a) and the Tomo-PIV, Figure 12(b). The u- and v-components of velocity are plotted along with the vorticity. The velocity scales on the line plots are the same, only the vorticity scales are different. The high speed jet of fluid expelled from the synthetic jet should have a flat topped velocity profile until it experiences enough shear with the ambient fluid to reach a fully developed flow profile. The Dual Plane PIV profile exhibits the expected flat top profile. However, the Tomo-PIV v-component profile peaks on the outer edges with a low velocity region in the middle. The difference in the centerline velocities is approximately 6 m/s, which corresponds to a 3 pixel error in displacement. A more significant difference is observed in the u-component of velocity. The Tomo-PIV u-component range is ±1 m/s compared to the ±4 m/s range Dual Plane PIV. The Tomo-PIV result shows that the u-component was not resolved through the vortex core, leading to the gross underestimate of the ω_z vorticity. The 3 m/s error in the under estimated u-component corresponds to a displacement error of 1.6 pixels. It appears that while there was sufficient seed particle concentration for the SPIV and Dual Plane PIV to accurately reconstruct the velocity in the vortex cores, there was not sufficient seed particle concentration in the vortex cores for the Tomo-PIV 3D particle field to be accurately reconstructed. Only the horizontal u-component of velocity was under predicted. The Tomo-PIV technique appears to be very sensitive to the local seed particle concentration.

As shown in Figure 11, even SPIV is capable of providing in-plane vorticity estimates. The main motivation for using the Dual Plane or Tomo-PIV technique is so that the out-of-plane vorticity can be computed. Figure 13 shows the in-plane vorticity as a contour map with velocity vectors along with an iso-vortcity magnitude surface which is computed using the root mean square of all three components of vorticity from the Dual Plane PIV data. Figure 13(a) shows the backside view of the same counter rotating vortices of the jet plume shown in Figure 11. However, the addition of the iso-vorticty surface information shows an interesting mushroom shaped outline of the synthetic jet's toroidal vorticity field. Figure 13(b) shows a front side view of the vorticity magnitude plot where the complete 3D mushroom shape of the flow vorticity iso-surface is readily apparent. The base of the mushroom is generated by the shear layer caused by the high speed jet plume. The top of the mushroom depicts the outline of the toroidal vortex. The outside edge of the toroidal vortex is slightly truncated due to the limited number of the measurement planes along the z-axis. The iso-vorticity surface plot shows the high fidelity information content available from the Dual Plane PIV technique.
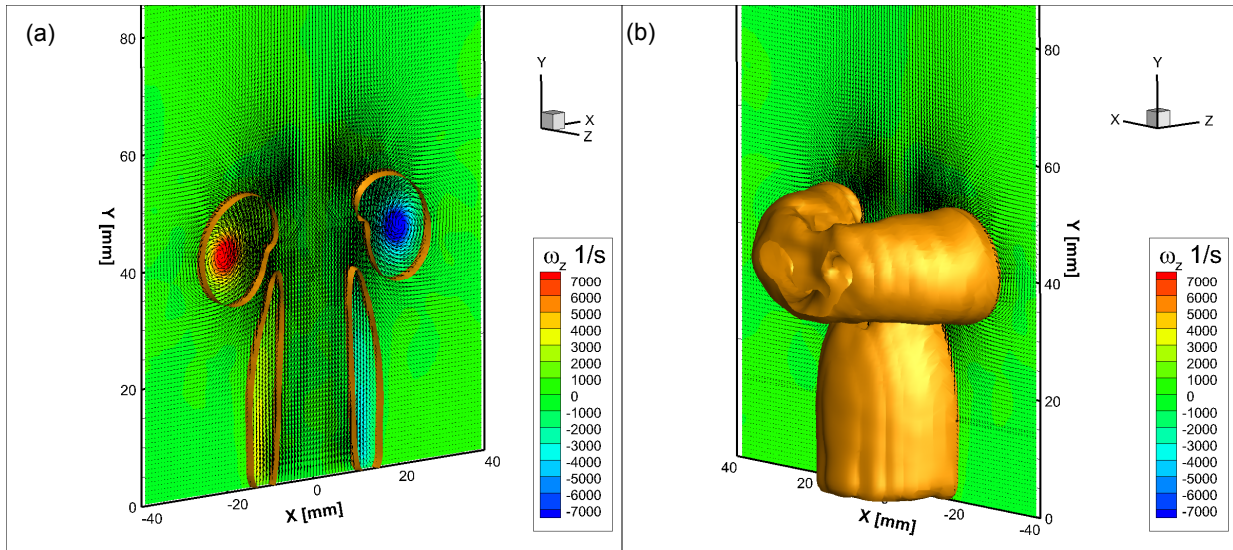
Figure 13.—Dual Plane PIV: (a) Map of both in-plane vorticity using color contours and iso-vorticity magnitude surface which outlines the regions of vorticity; (b) Backside view of the same dataset showing the 3D vorticity magnitude as an iso-vorticity surface. The strength of the out-of-plane vorticity estimates are similar to the in-plane measurements.
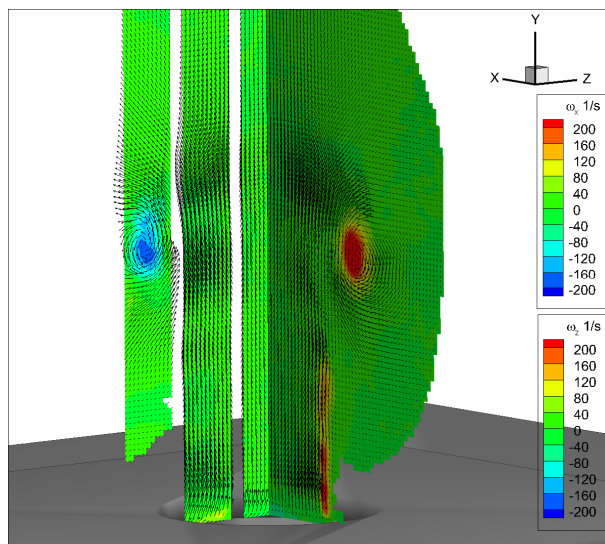

Figure 14.—Tomo-PIV map of both the in-plane vorticity ω_z and out-of-plane vorticity ω_x. The magnitude of the out-of-plane vorticity matches the in-plane value and the location of the vortex core is at the same radial location as the in-plane vortex core. The Tomo-PIV vorticity estimates are more than an order of magnitude lower than the SPIV and Dual Plane PIV results.

For comparison, the Tomo-PIV data was also used to illustrate its out-of-plane vorticity measurement capability. Figure 14 shows ω_z (computed from the in-light-sheet-plane u- and v-components of velocity) and ω_x (computed from the out-of-plane w- and in-plane y-components of velocity) on the x-axis and z-axis centerline planes, respectively. The data along the z-axis only exists within the Tomo-PIV reconstruction volumes, which do not overlap. The location of the vortex cores are the same which confirms the rotational symmetry of the data. The strength of the Tomo-PIV out-of-plane vorticity is similar to the in-plane values – which are still over an order of magnitude lower than the values measured using Dual Plane PIV.

In addition to not accurately extracting the magnitude of the flow vorticity, another disturbing feature in the Tomo-PIV data is in the inaccurate reconstruction of the flow gradients along the z-axis of the reconstruction volumes. Figure 15 shows horizontal plane (x-z-plane) slices through the high speed plume exiting the exhaust port on the synthetic jet. The slices are contours of velocity magnitude with velocity vectors overdrawn. A CAD model of the synthetic jet exit plane (gray region) is shown below the data slices. A red circle representing the actual exit port circumference is overdrawn on the data for clarity, while the dark gray circular region denotes the exit port of the synthetic jet. Figures 15(a) and (b) show slices through the Dual Plane PIV data at heights above the exit port corresponding to y = 1 mm and y = 8 mm, respectively. The SPIV data are not shown since they are identical to the Dual Plane result. The Dual Plane data show that for both locations above the exit plane of the synthetic jet, the cross-section of the high speed jet plume is round and inscribed within the diameter of the port, as expected. For the Tomo-PIV result shown in Figures 15(c) and (d), the magnitude of the velocity within the jet plume roughly matches the velocity in the Dual Plane PIV result for both the y = 1 and y = 8 mm planes.
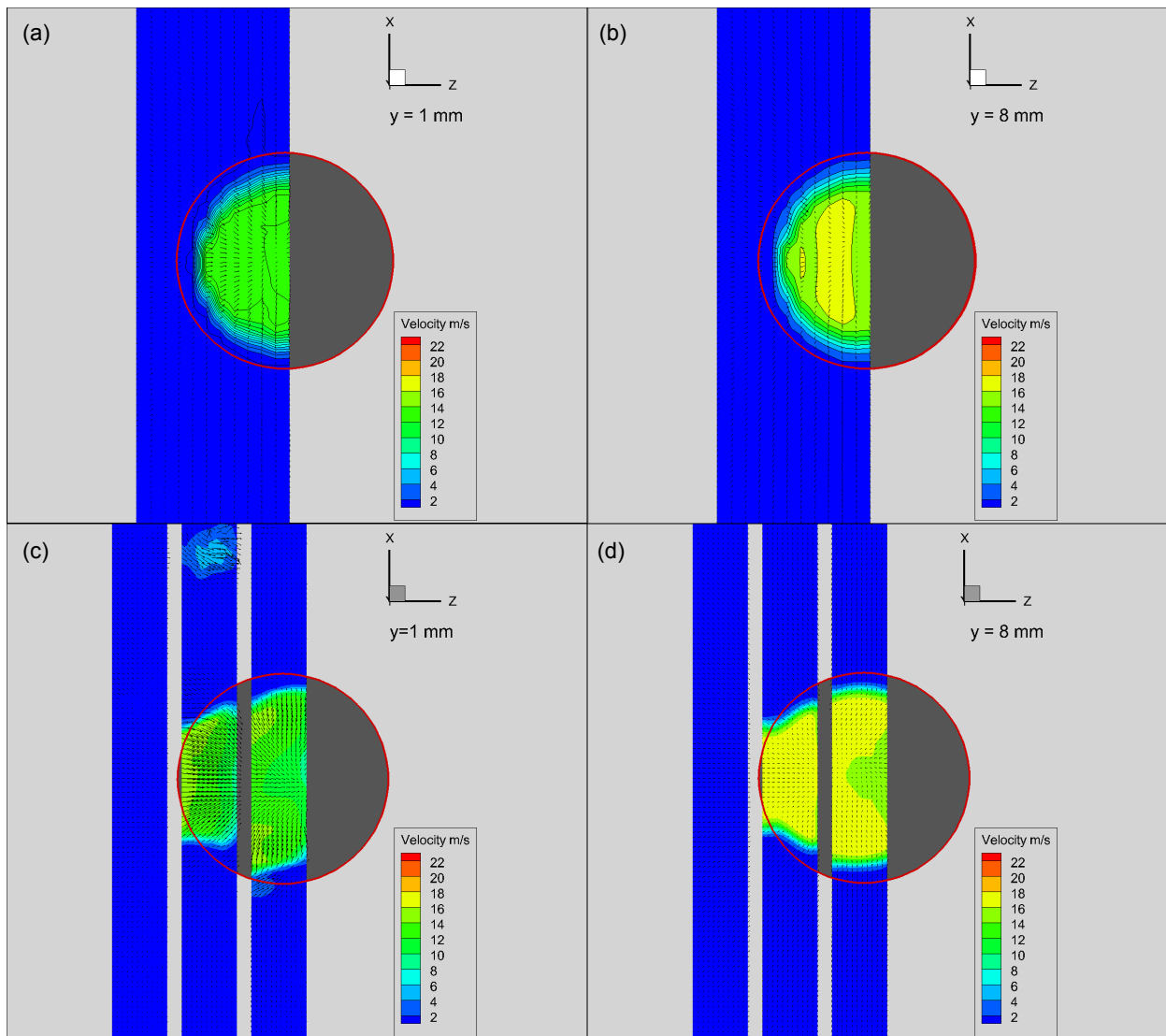

Figure 15.—Horizontal slices above the exhaust port plane through the 35 mm vortex height data set. Contours of velocity magnitude and velocity vectors are shown. Dual Plane PIV slices at: (a) y = 1 mm and (b) y = 8 mm. Tomo-PIV slices at: (c) y = 1 mm and (d) y = 8 mm. A red circle delineating the perimeter of the exhaust port is overdrawn on the data for clarity.

However, the Tomo-PIV reconstructed jet plume exiting the synthetic jet exhaust port is not round. The high speed jet plume is pear-shaped and extends beyond the back edge of the actual exhaust port, which is not physically possible. In addition to the apparent distortion in the shape and extent of the reconstructed velocity field, the width of the exhaust plume along the x-axis is somewhat smaller than the actual synthetic jet exhaust port diameter. The shear layer in the Tomo-PIV data is much thinner than in the Dual Plane result and starts further out into the jet. Whereas the Dual Plane data shows a more gradual gradient in velocity that extends out to the periphery of the exit port as the quiescent surrounding air is entrained by the jet.

The discrepancy in the Tomo-PIV data appears to be due to inaccuracies in reconstructing the 3D particle field in regions of high flow gradients. Close to the model exit at $y = 1$ mm flare light from the surface could be a concern. However the same distorted flow phenomena is observed at $y = 8$ mm above the exit plane, where there is certainly no flare light in the recorded Tomo-PIV data images. The jet plume exiting the exhaust port has a high velocity gradient in a cylindrical shape. The Tomo-PIV system appears to be incapable of accurately reconstructing the physical location and physical extent of the jet shear layer. The shape and location of the jet plume is not the only discrepancy observed in the Tomo-PIV data. Gradients in the vertical velocity component on the outside edge of the jet plume were under predicted in the Tomo-PIV data compared to the thin sheet techniques, violating the circular symmetry of the ejector plumes. Note the flatness of the underside of the Tomo-PIV jet plume vortex at the outermost ($z = 23$ to 17 mm) reconstruction domain in Figures 7(c) and 8(b). Another discrepancy is revealed when comparing the width of the intake flow at the exhaust port opening shown in Figure 10. The width of the high speed region of the plume is narrower in the Tomo-PIV result than in the Dual Plane result.

The recorded Tomo-PIV images were very uniformly seeded and there is no indication of any flow features in the images, which is ideal for any type of PIV measurement. Hence, there should be no issues caused by the flow seeding concentration. However, there are several factors contributing to these errors in the Tomo-PIV reconstructed velocity field, which are all traceable back to the limited number of views used in Tomo-PIV. The reconstructed particles are elongated along the z-axis due to the limited views. There is also limited shortening of the reconstructed particles along the y-axis due to all of the cameras being mounted in the same horizontal plane. The number of ghost particles is directly related to the limited number of views and particle concentration. The largest errors in the Tomo-PIV data were observed in regions of the flow with high velocity gradients.

Conclusions

Traditional 2-component PIV and Stereo PIV are accepted standards for making accurate planar flow field measurements. In this work two extensions of the basic technique, namely Dual Plane PIV and Tomo-PIV were investigated and demonstrated on a synthetic jet flow. These extensions of the basic technique offer the user the ability to compute out-of-plane flow field properties. The Dual Plane PIV technique provides reliable, high precision measurements since it is merely an implementation of two simultaneous SPIV systems. Tomo-PIV is capable of providing much higher data density reconstructed velocity fields than the thin sheet techniques, if that is a key requirement for a given test. In most real world experiments, the thick light sheet is still much smaller than the characteristic length scales of interest in the flow, which means Tomo-PIV provides too high of a data density over too small of an extent of the flow to be really useful. The objective of this study was to determine the viability and accuracy of the newer Tomo-PIV technique compared to the more traditional, thin sheet techniques. It was determined that image preprocessing of the raw image data before application of the tomographic reconstructions was not necessary, which is contrary to most other reported work. In many aspects the Tomo-PIV measurements agreed with the thin sheet SPIV and Dual Plane PIV results. However, both the in-plane and out-of-plane vorticity components computed from the Tomo-PIV were more than an order of magnitude lower than that obtained from either thin sheet technique. Measurement errors on the order of several pixels were observed in regions of high velocity gradients. Additionally, significant distortions were observed in the Tomo-PIV reconstructed high shear flow field near the synthetic jet exit port. These

distortions in the jet flow are artifacts of the 3D reconstruction used in Tomo-PIV most probably arising from the limited number of views. The flow fields were uniformly and well seeded for all of the experiments, hence the seed particle concentration is not considered a source for the errors observed. In Tomo-PIV there is generally less sensitivity to the depth component of the flow due to the limited number of views used to perform the reconstruction over s significant depth of the flow. This is not unexpected since it is difficult to compress the 3D particle field onto a small number (four) of 2D images and still be able to accurately reconstruct the 3D particle field. The MART does an admirable job reconstructing the flow from the limited number of views. However, these Tomo-PIV measurements are still inferior to thin sheet based techniques.

Dual Plane PIV offers all of the same flow field properties as Tomo-PIV, albeit at a lower data density (number of measurement planes). Similar data density can be acquired using Dual Plane PIV with a concomitant increase in the experiment run time. Dual Plane PIV is based on using two SPIV systems in a flow, so the hardware complexity is marginally higher than that required for Tomo-PIV. The Dual Plane PIV employs standard SPIV data reduction processes and can be completed using modest computation processing facilities in short order. Tomo-PIV requires merely the addition of a second pair of cameras to a standard stereo PIV setup and a thicker light sheet in order to acquire the data. However, the data processing requirements are daunting. High CPU core count pc with large amounts of memory and large hard drive space are required to process the Tomo-PIV reconstructions. Tomo-PIV data processing times are measured in weeks and months. The success of the Tomo-PIV measurements is intimately related to the flow seeding concentration and SNR of the recorded images. The likelihood for successful measurements using Tomo-PIV is low, without considerable time and effort devoted to optimizing the flow seeding concentration. For the modest increase in the illumination and recording equipment requirements, Dual Plane PIV offers the same information as Tomo-PIV with a much faster data turn around and a much higher probability for success. If there is ample time and resources available to enable the parameters of the Tomo-PIV to be optimized, then this technique may be attractive. If however the experimental hardware runtime/cost/time is a consideration, Dual Plane PIV may be the more attractive technique for ensuring that successful flow field measurements are obtained and processed in the shortest amount of time.

References

1. Scarano, F., 2013, "Tomographic PIV: principles and practice," *Meas. Sci. Technol.* 24, pp. 1–27.
2. Kaehler, C.J., Kompenhans, J., 1999, "Multiple plane stereo PIV: technical realization and fluid – mechanical significance," Proceedings of the 3rd International Workshop on PIV, Santa Barbara, September 16–18.
3. Hu, H., Saga, T., Kobayashi, T., Taniguchi, N., Yasuki, M., 2001, "Dual-plane stereoscopic particle image velocimetry: system setup and its application on a lobed jet mixing flow," *Exp. in Fluids*, 31, pp. 277–293.
4. Wernet, M.P., 2016, "Application of TomoPIV in a Large Scale Supersonic Flow Facility," submitted for publication in Experiments in Fluids, February, 2016.
5. Wernet, M.P., Wroblewski, A.C., Locke, R.J., 2016, "A Dual-Plane PIV Study of Turbulent Heat Transfer Flows," NASA/TM—2016-219074.
6. Paxson, D.E., Wilson, J., and Dougherty, K.T., 2002, "Unsteady Ejector Performance: An Experimental Investigation Using a Pulsejet Driver," AIAA Paper 2002–3915, July.
7. Paxson, D.E., Wernet, M.P. and John, W.T., 2007, "Experimental Investigation of Unsteady Thrust Augmentation Using a Speaker-Driven Jet," *AIAA Journal*, Vol. 45, No. 3, pp. 607–614.
8. Prasad, A.K., Adrian, R.J., 1993, "Stereoscopic particle image velocimetry applied to liquid flows," *Exp. in Fluids* 15, pp. 49–60.
9. Bjorkquist D.C., 2002, "Stereoscopic PIV calibration verification," *Proceedings of the 11th international symposium on application of laser techniques to fluid mechanics*, Lisbon, Portugal, July.

10. Scarano, F., 2002, Iterative image deformation methods in PIV. *Meas. Sci. Technol.*, Vol. 13, pp. R1-R19.

11. Taylor, J.R., An Introduction to Error Analysis, University Science Books, Oxford University Press, Mill Valley, CA., 1982, pp. 142–144.

12. Decker, A.J., Izen, S.H., 1992, "Three-dimensional computed tomography from interferometric measurements within a narrow cone of views," *Appl. Opt.*, Vol 31, No. 36, pp. 7696–7706.

13. Elsinga, G.E., van Oudheusden, B.W. and Scarano, F., 2006, "Experimental assessment of tomographic-PIV accuracy," *13th Int. Symp. On Applications of Laser Techniques to Fluid Mechanics* (Lisbon, Portugal).

14. Buchner, A-J., Buchmann, N.A.; Kilany, K., Atkinson, C., Soria, J., 2012. "Stereoscopic and tomographic PIV of a pitching plate," *Exp. in Fluids* 52, pp. 299–314.

15. Wernet, M.P., Pline, A., 1993, "Particle displacement tracking technique and Cramer-Rao lower bound error in centroid estimates from CCD imagery," *Exp. in Fluids* 15, pp. 295–307.

16. Melling, A., 1997, "Tracer particles and seeding for particle image velocimetry," *Meas. Sci. Technol.* 8, pp. 1406–1416.